Resolving ICME Turbulence with a Planetary Spacecraft Radio Link

An uncertainty-aware reanalysis of the 6 April 2015 Mars Express event | Research Article

Anonymous manuscript for peer review

Prepared 14 August 2026

Target journal: *Space Weather*
Manuscript type: Research Article
Running title: Radio sounding of an ICME
Author details: Withheld in this review draft; insert names, affiliations, ORCIDs, and corresponding-author information before submission.
Status: Original reanalysis manuscript; not peer reviewed.

> **Scope note.** This study reanalyzes published, numerical Mars Express radio measurements and cross-validates them against frozen NASA DONKI and JPL Horizons records. It does not claim access to the unavailable raw baseband recordings. All primary conclusions are calibration-invariant; an ambiguity in the published absolute-TEC conversion is disclosed and isolated in Appendix A.

Key Points

- Matched controls show a 3.0–5.1-fold increase in phase-scintillation amplitude, a 2.8–4.6-fold increase in Doppler noise, and a 15–16-fold increase in spectral-peak power during the ICME.
- A blind three-regime segmentation resolves a 60 ± 20 min high-scattering layer; two intercontinental stations track the same evolution (CCC = 0.925), while phase and Doppler noise co-vary at Badary ($r = 0.858$, permutation $p = 0.0024$).
- DONKI launch timing and the modeled 0.50–0.60 AU radio-path crossing imply a path-averaged speed of 686 km s^{-1} (95% interval 613–760) and a radial-equivalent layer thickness of 0.016 AU (0.011–0.023).

Plain Language Summary

Radio waves from a spacecraft carry an imprint of every plasma structure they cross. We use that imprint to revisit a coronal mass ejection that crossed the Earth–Mars Express radio path on 6 April 2015. Fourteen 20 min measurements from radio telescopes in Russia and South Africa show that the signal phase and Doppler frequency became far more variable than on nearby quiet days. A statistical change-point search, performed without prescribing the transition times, identifies a one-hour region of especially strong turbulence. The two telescopes observed nearly the same evolution when they operated simultaneously, which is difficult to explain by local weather or instrumentation. Combining the radio timing with NASA's CME catalog and ephemeris geometry gives an average propagation speed near 686 km s^{-1} and a turbulent-layer thickness near 0.016 astronomical unit, about 2.5 million km. The radio data constrain turbulence and spatial scale robustly, but they do not by themselves determine bulk electron density. We therefore report density-independent measurements and explicitly quarantine an inconsistent absolute calibration in the source article. This approach shows how routine deep-space communications can become a distributed monitor of solar-wind transients.

Abstract

Planetary spacecraft radio links provide long, otherwise inaccessible chords through the inner heliosphere, but physical inference from isolated scintillation events is vulnerable to sparse sampling, terrestrial systematics, and calibration assumptions. We conduct an uncertainty-aware reanalysis of the interplanetary coronal mass ejection (ICME) intercepted by the two-way 8.421 GHz Mars Express link on 6 April 2015. The analysis uses 14 published 20 min scans from Badary and Hartebeesthoek, four matched quiet-day sessions, a frozen NASA DONKI catalog record, and independent JPL Horizons geometry. Relative to the nearest same-station controls, phase-scintillation amplitudes increased by factors of 2.99 (95% interval 2.17–4.10) and 5.11 (4.20–6.19), Doppler noise by 2.76 (2.25–3.38) and 4.57 (3.95–5.29), and spectral peaks by factors of 15.2 and 16.4. At Badary, phase scintillation and Doppler noise co-varied ($r = 0.858$; 200,000-permutation $p = 0.0024$). Exhaustive Bayesian-information-criterion segmentation favors three regimes over the best two-regime representation by ΔBIC = 7.71, isolating a 60 ± 20 min high-scattering layer whose phase-variance proxy is 2.37 times that of its ICME flanks. Simultaneous station measurements agree closely (concordance correlation coefficient 0.925), although only four pairs limit formal significance. Combining the DONKI time at 21.5 solar radii with the modeled 0.50–0.60 AU crossing yields a path-averaged speed of 686 km s^{-1} (613–760), a layer thickness of 0.016 AU (0.011–0.023), and a full disturbed-width lower bound of 0.055 AU. The phase-spectrum slope, -2.801 ± 0.065, is only marginally steeper than the Kolmogorov value. Absolute electron content is not inferred because the archived conversion is internally non-reproducible. The results establish a transparent, calibration-resistant route from operational radio tracking to CME turbulence, speed, and scale.

Keywords: coronal mass ejection; solar wind; radio science; Mars Express; phase scintillation; Doppler tracking; heliospheric remote sensing

1. Introduction

Coronal mass ejections (CMEs) reorganize coronal magnetic flux and inject magnetized plasma into the heliosphere. Their interplanetary counterparts can drive shocks, compress pre-existing solar wind, and alter the radiation and plasma environments encountered by spacecraft and planets (Cane & Richardson, 2003; Chen, 2011). White-light coronagraphy provides indispensable near-Sun morphology, while heliospheric imaging and in situ monitors constrain selected trajectories. A persistent observational gap nevertheless remains: a single imager integrates Thomson-scattered brightness along a broad line of sight, and an in situ monitor samples only the plasma that reaches its position. Radio links to planetary spacecraft offer a complementary pencil beam through regions that are not routinely instrumented.

Propagation through a fluctuating electron plasma advances the carrier phase and introduces stochastic phase and frequency variations. For a coherent link, the frequency perturbation is the time derivative of the plasma-imprinted phase,

$$\delta f(t) = \frac{1}{2\pi}\frac{d\phi(t)}{dt}.$$

The relation makes phase scintillation and Doppler noise physically connected but operationally distinct diagnostics. At fixed carrier frequency and approximately fixed geometry, phase variance is proportional to a path-integrated density-fluctuation measure; it is not, without additional assumptions, a direct measurement of the mean electron column. Solar-wind phase scintillation can dominate the precision-noise budget of deep-space Doppler tracking (Armstrong, 1998). Conversely, that navigation noise is a remote-sensing signal.

Spacecraft radio sounding has progressed from conjunction experiments to systematic open-loop tracking. The PRIDE processing chain extracts narrowband Doppler and residual phase from signals received by VLBI-class telescopes (Duev et al., 2012; Molera Calvés et al., 2014; Bocanegra-Bahamón et al., 2018). A seven-year Mars Express campaign found stable, approximately power-law phase spectra over a wide range of elongations (Kummamuru et al., 2023), and more recent work has formalized phase structure functions and multi-spacecraft-in-beam localization (Edwards et al., 2025, 2026). These developments make operational telecommunications links increasingly credible as a component of heliospheric monitoring.

The 6 April 2015 event is a particularly valuable test. Molera Calvés et al. (2017) reported that an ICME crossed the Mars Express–Earth radio path near 0.5–0.6 AU. Badary (Bd) observed ten consecutive scans; Hartebeesthoek (Ht) supplied four simultaneous scans near the end of the session. Adjacent quiet-day measurements at the same stations provide controls, while coronagraph catalogs and a WSA–ENLIL solution identify the solar transient. The original study established the detection and proposed an internal density enhancement. Its archived numerical tables now permit a more explicit uncertainty analysis, even though the original raw-data repository no longer permits anonymous access.

Here we ask four narrowly testable questions. First, do independent radio diagnostics distinguish the event from matched controls after scan-to-scan variability is propagated? Second, does the time series require internal regimes without prescribing their boundaries? Third, are the simultaneous station measurements sufficiently concordant to disfavor local systematics? Fourth, what speed and spatial scales follow when radio timing is combined with independently archived CME and ephemeris data? We intentionally separate calibration-invariant observables from an absolute total-electron-content (TEC) mapping. This distinction produces a conservative physical characterization and exposes exactly which conclusions would survive a future reprocessing of the raw voltage data.

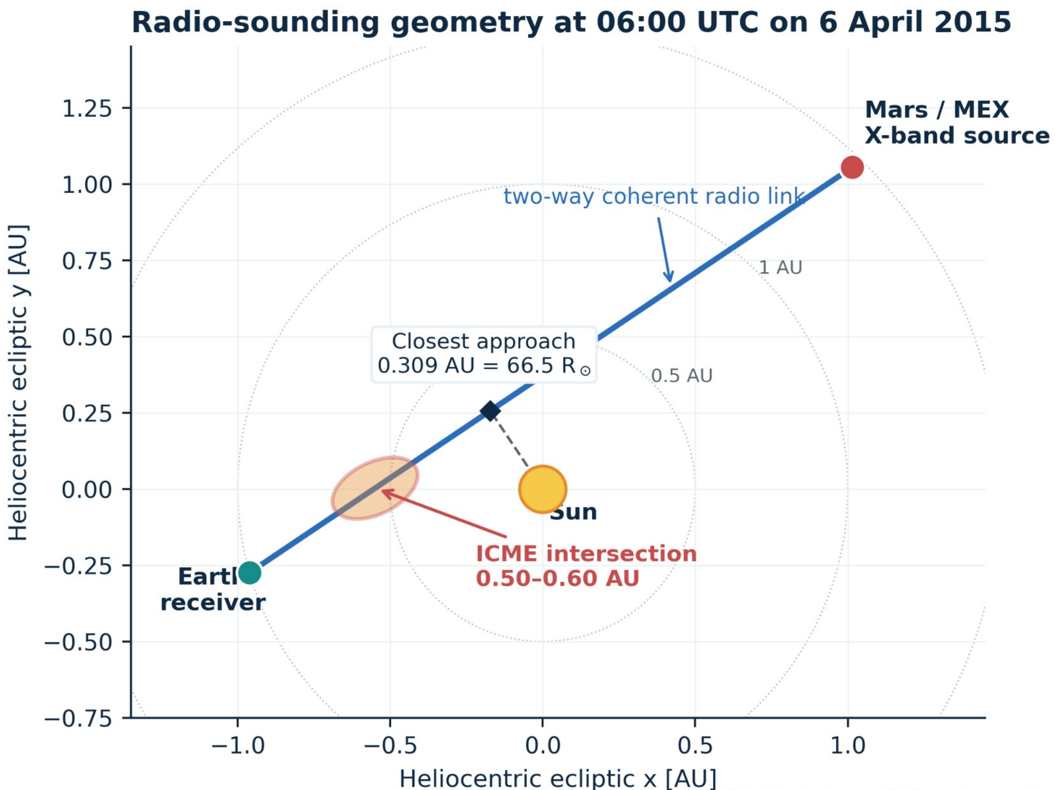

The 6 April 2015 Earth–Mars Express radio path in the heliocentric ecliptic plane. Earth and Mars states are from JPL Horizons at 06:00 UTC. The line of sight passed 0.309 AU (66.5 solar radii) from the Sun. The illustrated ICME intersection is the Earth-side 0.55 AU crossing consistent with the published WSA–ENLIL solution; the ellipse is schematic and not a fitted flux-rope boundary.

2. Data and Event Geometry

2.1 Radio observations

We transcribed the numerical values in Tables 2 and 4 of Molera Calvés et al. (2017) directly into machine-readable files. No values were digitized from plots. The event data comprise ten 20 min Bd scans from 05:20 through 08:20 UTC and four Ht scans from 07:20 through 08:20 UTC. A scan beginning at 08:20 covers the interval to approximately 08:40, so the published sequence spans 200 min. Each record includes the phase scintillation index σ_{Sc}, its reported measurement uncertainty, a session-level spectral slope and peak, a noise-floor estimate, Doppler noise, and carrier signal-to-noise ratio.

The source table labels the per-scan Doppler column as hertz, but its numerical values (14.93–26.05) and the session summaries (means of 19.1 and 19.7 mHz) establish that the per-scan unit is millihertz. Treating those entries as hertz would create a factor-of-1000 discontinuity inside the same table. We therefore normalize the unit to mHz and preserve the original numbers. This is a unit repair, not a rescaling of values.

Four non-event sessions supply matched controls: Ht on 3 and 4 April and Bd on 9 April, with 3, 3, and 14 scans, respectively. For the primary event/control contrasts we use the temporally nearest same-station session—Ht on 4 April and Bd on 9 April. The 4 April Ht control also has the larger of the two Ht background amplitudes and is therefore conservative. A sensitivity check using both Ht control days does not change the direction or interpretation of any contrast.

Station/session	Scans	Phase amplitude [rad]	Doppler noise [mHz]	Spectral peak [rad² Hz⁻¹]	Role
Ht, 4 April	3	0.65 ± 0.07	6.9 ± 0.4	1,153	Primary Ht control
Ht, 6 April	4	1.96 ± 0.59	19.1 ± 3.8	17,477	ICME
Bd, 6 April	10	2.25 ± 0.56	19.7 ± 4.0	12,550	ICME
Bd, 9 April	14	0.44 ± 0.10	4.3 ± 0.6	763	Primary Bd control

Table 1. Session summaries used for matched contrasts. Values after ± are published scan-to-scan dispersions, not formal posterior uncertainties. Ht = Hartebeesthoek; Bd = Badary.

2.2 External CME and ephemeris records

The NASA Community Coordinated Modeling Center's DONKI record `2015-04-04T23:36:00-CME-001` identifies a LASCO C2/C3 transient associated with the event. Its most-accurate catalog analysis places the leading edge at 21.5 solar radii at 02:45 UTC on 5 April, with a speed of 1,090 km s^{-1}, latitude −25°, longitude −29°, and half angle 36°. Molera Calvés et al. (2017) independently report a CACTus onset at 23:48 UTC on 4 April and a modeled line-of-sight crossing around 0.50–0.60 AU early on 6 April. The 12 min onset difference is immaterial because our transit calculation begins at the DONKI 21.5-solar-radius time.

JPL Horizons gives a geocentric Mars Express range of 2.38217 AU and an apparent solar elongation of 17.9916° at 06:00 UTC on 6 April. Mars-center values differ negligibly (2.38223 AU; 17.9902°). Straight-line minimization of the heliocentric Earth and Mars vectors yields a solar impact parameter of 0.30910 AU, or 66.47 solar radii (Figure 1). The original article reports 2.39 AU and 17.23°; the range agrees after rounding, while the 0.76° elongation difference remains unexplained. Repeating our geometry with either elongation does not affect the event/control statistics or the kinematic calculation, which uses the modeled radial crossing interval.

2.3 Provenance and access boundary

Table 2 distinguishes direct numerical observations, archived external records, and derived quantities. The published article links to a Bitbucket repository for its data; that URL required authentication when checked on 14 August 2026. We therefore do not represent raw baseband or residual-phase samples as available. The present evidence base is nevertheless more informative than plot digitization: every analyzed radio value is a printed numerical entry, the external JSON and ephemerides are frozen in the reproducibility package, and checksums are supplied.

Asset	Provider	Level used	Persistent locator	Use in this study
MEX radio scans and session controls	Molera Calvés et al. (2017)	Published numerical Tables 2 and 4	DOI 10.1002/2017SW001701; CaltechAUTHORS record z773c-3ny24	Primary radio inference
CME catalog snapshot	NASA CCMC DONKI	Public JSON record	2015-04-04T23:36:00-CME-001	Launch/21.5-$R_{\odot}$ timing and speed
MEX/Mars observer ephemeris	NASA/JPL Horizons	API observer tables	Target −41 and 499	Range and elongation validation
Earth and Mars heliocentric states	NASA/JPL Horizons	API vector tables	Targets 399 and 499	Figure 1 and impact parameter
WSA–ENLIL crossing interval	Molera Calvés et al. (2017) / NASA CCMC	Published model result	0.50–0.60 AU	Kinematic interval, explicitly conditional

Table 2. Data provenance. Retrieval date for all web services and repository files: 14 August 2026 UTC.

3. Methods

3.1 Radio observables and calibration-resistant contrasts

We treat σ_{Sc} as an empirical phase-fluctuation amplitude and the squared amplitude as a scattering-strength proxy. For matched geometry and frequency, the event/control ratio

$$Q_\phi = \left(\frac{\overline{\sigma}_{Sc,event}}{\overline{\sigma}_{Sc,control}} \right)^2$$

is invariant to any common multiplicative phase-to-TEC calibration. It measures the enhancement of phase variance, not the enhancement of bulk electron density. Spectral-peak and Doppler ratios are likewise dimensionless and do not require an absolute plasma-column model.

The session table reports a mean and scan-to-scan standard deviation. To propagate uncertainty in the session mean, we use $SE = s/\sqrt{n}$ and approximate each positive mean with a lognormal distribution matched to that mean and SE. We draw 250,000 independent event/control pairs using a fixed seed and report medians with central 95% intervals. This model treats scans as exchangeable samples of a session. Because adjacent 20 min scans may be autocorrelated, the intervals should be interpreted as conditional precision rather than a complete systematic-error budget. Spectral peaks have no published uncertainty; their ratios are descriptive.

3.2 Blind temporal segmentation

We search all admissible one-, two-, and three-regime piecewise-constant models of the ten Bd phase-scintillation measurements. Each regime contains at least two scans. For a model with K regimes, residual sum of squares SSE, and $n = 10$, the Bayesian information criterion is

$$BIC = n \ln(SSE/n) + (K+1) \ln n,$$

where $K+1$ counts the segment means and common residual variance (Schwarz, 1978). Enumerating every partition avoids optimizer dependence. A 20,000-draw parametric bootstrap uses the preferred model's residual variance to quantify boundary stability. The analysis is blind in the limited but important sense that no CME substructure times are supplied to the algorithm.

3.3 Cross-observable and cross-station validation

We compute Pearson's r between Bd phase scintillation and Doppler noise and obtain a two-sided permutation probability from 200,000 randomized pairings. For the four simultaneous Ht–Bd scans, we report Pearson's r, Lin's concordance correlation coefficient (CCC), and the mean Ht-minus-Bd bias (Lin, 1989). With only $4! = 24$ unique permutations, the smallest attainable conventional two-sided significance level is coarse; we therefore describe concordance and disclose the exact permutation probability rather than treating the four pairs as a stand-alone hypothesis test.

3.4 Spectral slope

The published session phase-power slopes are −2.828 ± 0.079 at Bd and −2.744 ± 0.114 at Ht. We form an inverse-variance mean and compare it with the frozen-flow Kolmogorov phase-spectrum expectation, $-8/3$. The two values share the same heliospheric event and may contain common modeling systematics; their inverse-variance error is therefore a conditional statistical uncertainty.

3.5 Transit speed and radial-equivalent scale

The path-averaged speed from 21.5 solar radii to the radio intersection is

$$v_{tr} = \frac{r_{cross} - 21.5 R_\odot}{t_{cross} - t_{21.5 R_\odot}}.$$

We draw r_{cross} uniformly over the published 0.50–0.60 AU interval, set $t_{21.5 R_\odot}$ to the DONKI time 02:45 UTC on 5 April, and allow t_{cross} to vary uniformly by ±20 min around 06:00 UTC on 6 April. The 20 min range reflects the radio cadence, not a DONKI timing error. The resolved-layer duration is 60 min because three consecutive 20 min scans occupy the preferred middle regime. We use a conservative uniform 40–80 min sensitivity interval. The radial-equivalent thickness is $L = v_{tr} \Delta t$. It is the scale advected past the line of sight under a frozen-pattern approximation; it is not a deprojected flux-rope chord. The continuously disturbed 05:20–08:40 record supplies a 200 min lower bound on the total disturbed radial extent.

4. Results

4.1 Three independent radio contrasts detect the transient

The event is exceptional under every reported radio diagnostic (Figure 4). At Ht, the phase-amplitude ratio relative to 4 April is 2.99 (95% interval 2.17–4.10), and the Doppler ratio is 2.76 (2.25–3.38). At Bd, the corresponding ratios relative to 9 April are 5.11 (4.20–6.19) and 4.57 (3.95–5.29). Squaring the phase ratios gives scattering-strength proxies of 8.93 (4.73–16.84) and 26.08 (17.66–38.36). Session spectral peaks increase by factors of 15.16 and 16.45. Their agreement is notable because phase amplitude, frequency noise, and a Fourier-domain peak respond differently to processing choices.

The source article reports variable weather during the control sessions, yet the clearest weather occurred during the most disturbed Ht session. It also reports no transmission anomaly from ESA operations. Weather and transmitter state therefore have the wrong sign or lack the required timing to explain all contrasts. This does not eliminate unmodeled systematics, but it shifts the burden from a single noisy statistic to three mutually consistent observables at two sites.

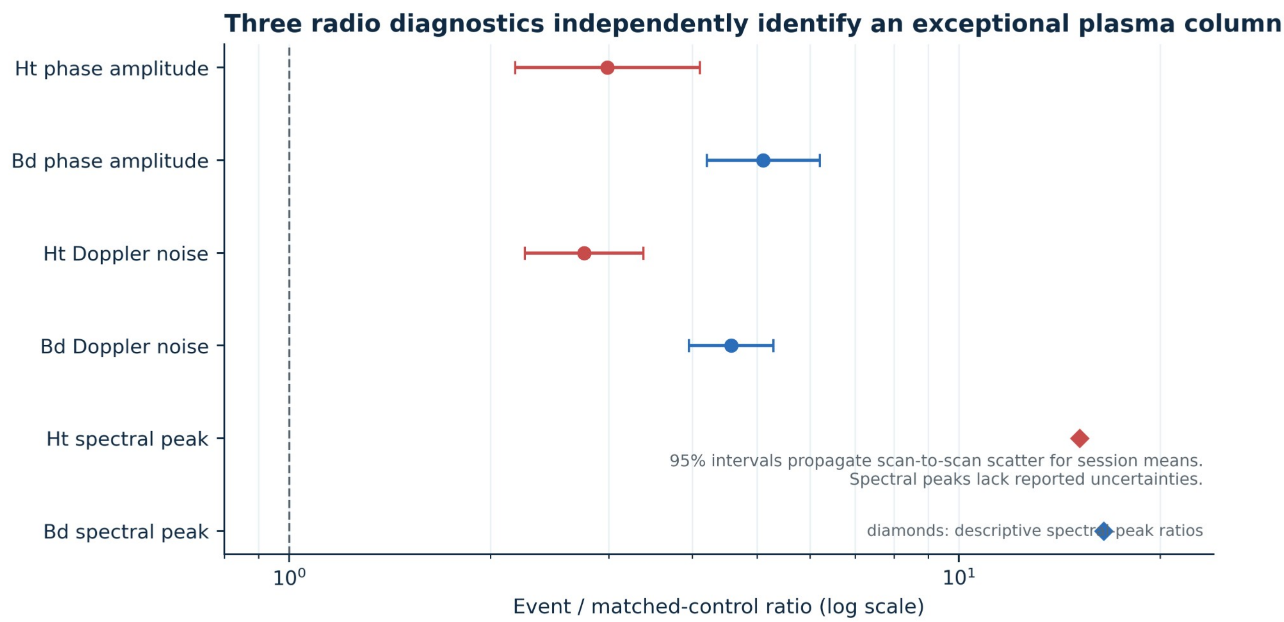

Event-to-control contrasts at each station. Phase and Doppler intervals propagate the published scan-to-scan dispersions to session means with positive lognormal sampling. Spectral-peak ratios are descriptive because no uncertainty was reported. The dashed line denotes no event enhancement.

4.2 The time series requires a high-scattering middle regime

The preferred three-regime Bd partition places boundaries after the 06:20 and 07:20 scans (Figure 2). Mean phase amplitudes are 2.022 rad before the first boundary, 2.967 rad in the 06:40–07:20 middle regime, and 1.832 rad afterward. The best BIC values are −6.90, −7.28, and −14.99 for one, two, and three regimes, respectively. Thus the three-regime description is favored over the best two-regime model by ΔBIC = 7.71, conventionally strong evidence on the BIC scale. In the parametric bootstrap the exact pair of boundaries is recovered in 68.8% of draws and both boundaries fall within one scan of the observed solution in 96.2%.

Relative to the mean of the two ICME flanks, the middle regime has a 1.54-fold phase amplitude and a 2.37-fold phase-variance proxy. This is internal contrast within a continuously disturbed session; it does not reuse the quiet-day controls. The result therefore supports a localized enhancement in density turbulence within the larger ICME disturbance. Calling that layer a magnetic cloud or a specific shock/sheath component would require magnetic-field or in situ plasma information that the radio data do not contain.

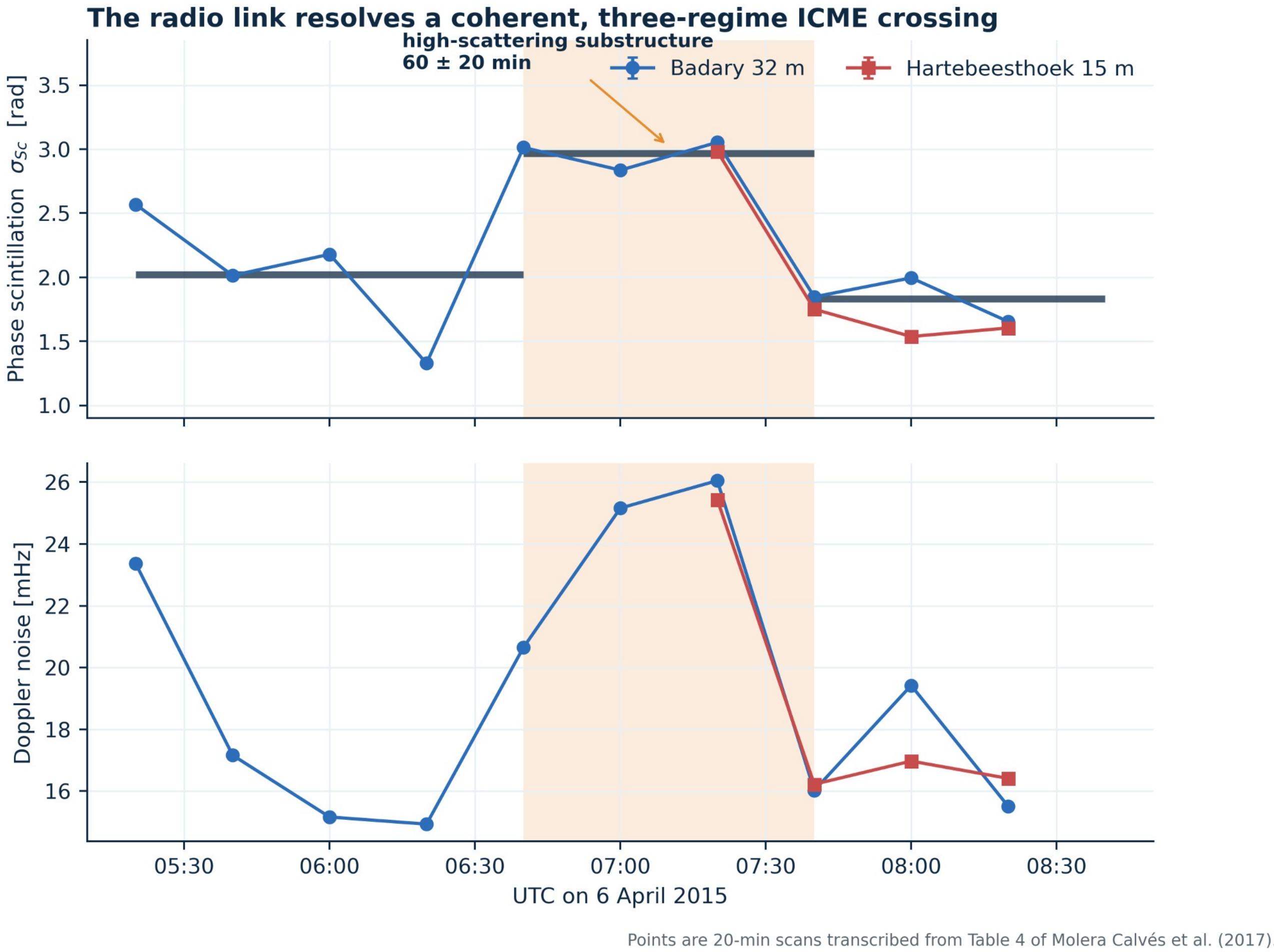

Top: phase scintillation for all 14 scans, with BIC-selected Bd segment means in dark horizontal bars. Bottom: Doppler noise. The orange interval marks the three-scan high-scattering regime. Reported phase-measurement errors are smaller than the plotting symbols; the larger variations are physical or systematic scan-to-scan changes.

4.3 Phase and Doppler fluctuations co-vary

Across the ten Bd scans, phase scintillation and Doppler noise correlate at $r = 0.858$. Only 0.24% of 200,000 random pairings produce an absolute correlation at least this large ($p = 0.0024$). The correlation is expected from $\delta f \propto d\phi / dt$, but it is not guaranteed: a single phase standard deviation and a Doppler-noise summary weight temporal frequencies differently. Their co-variation strengthens the inference that the central regime is a genuine propagation disturbance.

The four simultaneous scans give Ht–Bd $r = 0.960$ and CCC = 0.925. Ht is lower by 0.169 rad on average; Bland–Altman limits calculated from four differences are −0.549 to 0.211 rad. The largest mismatch occurs at 08:00. The remaining time evolution, including the sharp decline between 07:20 and 07:40, is reproduced at both stations. The exact station-pair permutation probability is 0.167 because the sample admits only 24 orderings, so the numerical concordance is compelling descriptively but underpowered inferentially. The intercontinental replication nevertheless makes a local receiver fault or tropospheric cell an implausible sole explanation.

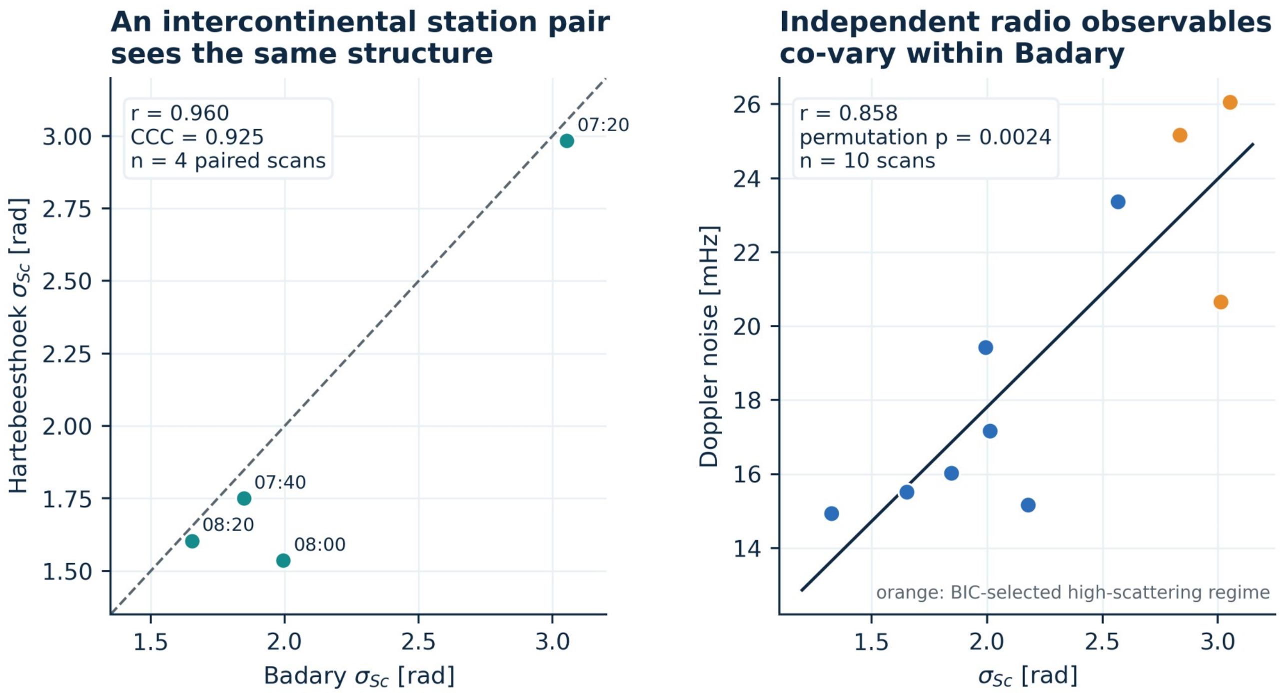

Left: simultaneous phase-scintillation measurements at Badary and Hartebeesthoek with a 1:1 reference. Right: Badary phase scintillation versus Doppler noise; orange marks the BIC-selected middle regime. The station agreement is descriptive because only four paired scans are available, whereas the within-Badary phase–Doppler association is tested by permutation.

4.4 The spectrum is close to, but slightly steeper than, Kolmogorov

The inverse-variance mean phase-power slope is -2.801 ± 0.065. It is steeper than $-8/3$ by 2.06 conditional standard errors (Figure 6). That is marginal evidence, not a robust rejection of a Kolmogorov cascade: only two session-level slopes are available, the fit frequency interval cannot be revisited without spectra, and both stations sample the same evolving plasma. The result is consistent with a near-Kolmogorov turbulent medium while allowing intermittency, anisotropy, an evolving outer scale, or processing-window effects. It also lies within the broader behavior reported for long Mars Express campaigns (Molera Calvés et al., 2014; Kummamuru et al., 2023).

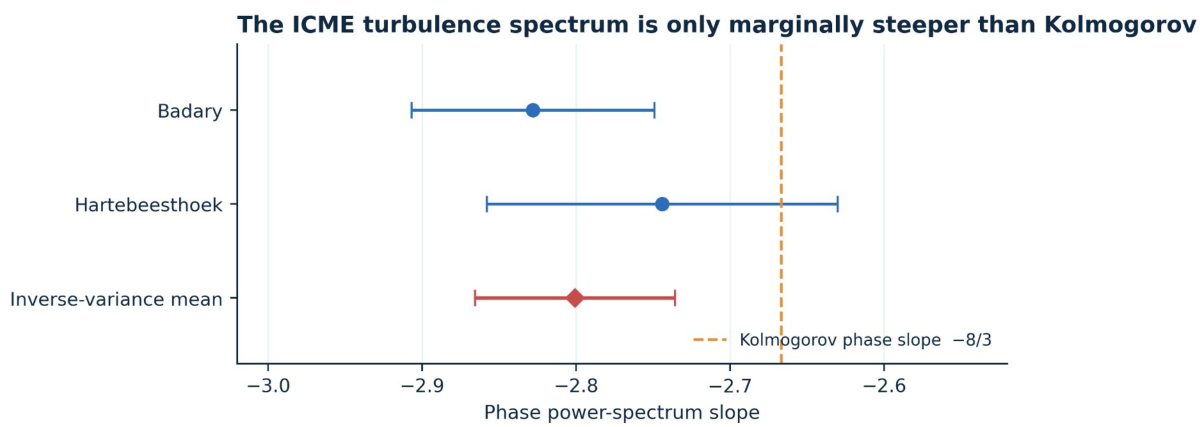

Published phase-power spectral slopes and their inverse-variance mean. The dashed reference is the frozen-flow Kolmogorov phase slope, −8/3. Error bars are the published conditional fit uncertainties.

4.5 Speed, layer thickness, and full-width lower bound

The DONKI leading-edge speed at 21.5 solar radii is 1,090 km s^{-1}. Propagation from that radius and time to a 0.50–0.60 AU crossing near 06:00 UTC yields a median path-averaged speed of 686 km s^{-1} and a central 95% interval of 613–760 km s^{-1} (Figure 5). The result agrees with the approximately 700 km s^{-1} WSA–ENLIL speed quoted for the crossing by Molera Calvés et al. (2017). The 37% reduction from the DONKI speed is consistent with deceleration toward the ambient flow, although catalog projection, front curvature, and the fact that the radio chord may sample a flank prevent a unique drag inference.

Combining the speed distribution with a 40–80 min duration sensitivity interval gives a median radial-equivalent thickness of 0.0164 AU, with a 95% interval of 0.0109–0.0228 AU. In dimensional terms the median is 2.46×10^6 km. Because the link remains disturbed from the beginning of the first Bd scan through the end of the last, 200 min of radio coverage set a full disturbed-width lower bound of 0.0550 AU (0.0492–0.0610). The data do not capture entry into or exit from the global ICME, so no upper bound follows.

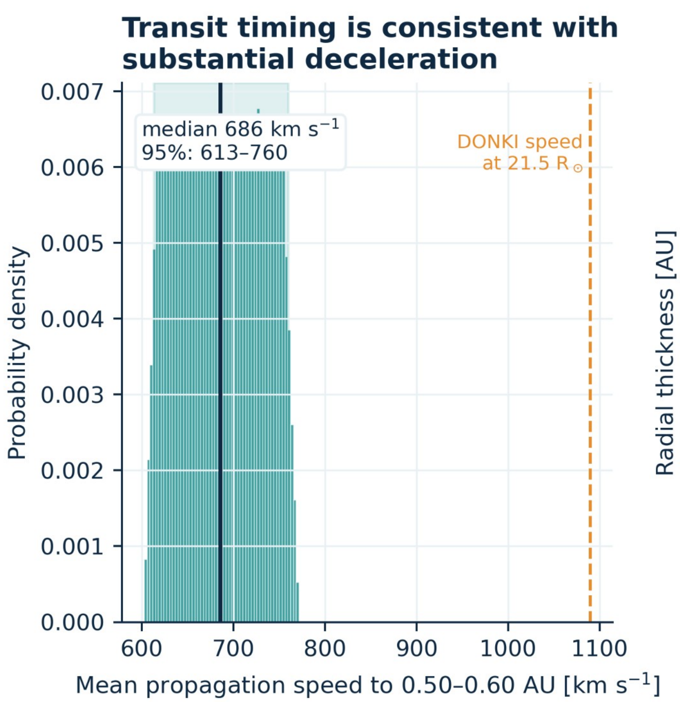

Left: path-averaged propagation speed inferred from the DONKI 21.5-solar-radius time and the 0.50–0.60 AU crossing interval. Right: radial-equivalent thickness as a function of the cadence-limited 40–80 min duration. Shading propagates crossing radius and ±20 min crossing-time uncertainty.

Physical quantity	Estimate	Uncertainty / bound	Dominant assumption
Path-averaged speed	686 km s⁻¹	613–760 km s⁻¹ (95%)	Crossing at 0.50–0.60 AU; ±20 min
High-scattering duration	60 min	40–80 min sensitivity	20 min scan cadence
Radial-equivalent layer thickness	0.0164 AU	0.0109–0.0228 AU (95%)	Frozen advection; no deprojection
Full disturbed radial extent	≥0.0550 AU	0.0492–0.0610 AU for speed uncertainty	Event extends beyond 200 min record
Internal phase-variance contrast	2.37×	Model-defined, calibration-invariant	Three-regime Bd segmentation
Phase spectral slope	−2.801 ± 0.065	Conditional 1σ	Two session-level fits

Table 3. CME properties supported by the radio, catalog, and geometry data. Intervals are conditional on the stated assumptions and are not full systematic-error bounds.

5. Discussion

5.1 What the radio link measures

The strongest inference is not a bulk density. It is a structured enhancement of electron-density fluctuations along a narrow line of sight. Three facts support that statement: the phase and Doppler diagnostics increase together, an independently selected central regime carries 2.37 times the phase-variance proxy of its ICME flanks, and the latesession decline is reproduced by two widely separated receivers. These are precisely the benefits of a spacecraft carrier over a natural compact source: a bright, narrow tone enables high-cadence phase and Doppler tracking with well-characterized transmitting hardware.

The radial-equivalent layer thickness is also unusually direct. Once an advection speed is supplied, the temporal interval translates into a spatial scale without converting phase to TEC. The inferred 0.011–0.023 AU interval overlaps the 0.014 AU estimate in the original event study, but the present interval makes the cadence and speed assumptions explicit. The continuously disturbed width of at least 0.055 AU separates the resolved internal layer from the larger ICME envelope.

The method complements, rather than replaces, white-light and in situ observations. A coronagraph constrains the global front and launch kinematics; the radio link resolves turbulence on a particular chord; an in situ monitor measures local plasma and magnetic field. Joint inversions could distinguish shock, sheath, flux-rope, and trailing-flow contributions. The 2026 multi-spacecraft-in-beam demonstration by Edwards et al. shows how common-mode phase patterns and time lags can additionally localize a moving scattering screen. The 2015 geometry lacks simultaneous spacecraft beams, but its dual-station coherence is an early form of the same redundancy.

5.2 Calibration audit and why bulk density is withheld

Molera Calvés et al. (2017) present an empirical conversion between σ_{Sc} and TEC. For the stated standard settings, their printed equation reduces to $TEC = 2K_s\sigma_{Sc}$ with $K_s = 2010$ TECU rad^{-1}. Applying that expression to their printed session indices (1.537 rad for Ht and 2.170 rad for Bd) gives 6,179 and 8,723 TECU. Table 2 instead gives 3,074 and 4,340 TECU, close to $K_s\sigma_{Sc}$ without the factor of two; the narrative/Table 5 values are 3,430 and 4,350 TECU. In addition, arithmetic means of the per-scan Table 4 values are 1.9685 and 2.2487 rad, not 1.537 and 2.170 rad. Appendix A reproduces the audit.

These discrepancies do not invalidate the radio detection. They do prevent an independent reader from identifying a unique absolute electron column from the archived numerical record. More fundamentally, an event-specific mapping from phase variance to mean TEC requires assumptions about the turbulence amplitude, inner and outer scales, effective screen location, solar-wind speed, and two-way correlation. The original authors themselves noted that their empirical K_s might differ inside an ICME. We therefore do not turn the published TEC excess into a local density; dividing a path-integrated, turbulence-calibrated quantity by the 0.016 AU layer thickness would create a falsely precise and likely unphysical result.

This conservative decision is scientifically productive. Every headline result in Table 3 is unchanged if the absolute phase-to-TEC scale is multiplied by two, if a different background density profile is adopted, or if future raw-data processing changes the mean phase offset. The paper thereby distinguishes *detection and structural inference*, which the available data support, from *bulk plasma inversion*, which they do not.

5.3 Implications for operational space-weather sensing

Deep-space networks already schedule coherent links, maintain frequency standards, and archive navigation observables. A radio-sounding product could be layered on that infrastructure with three operational additions: (1) routine open-loop or sufficiently high-rate closed-loop recording, (2) near-real-time detrending and phase-spectrum estimation with versioned calibration, and (3) geometric association with coronagraph/heliospheric-model ensembles. The 2015 case indicates that a single link can identify a several-hour disturbed interval and resolve an internal layer at 20 min cadence. A network of simultaneous planetary links would provide multiple chords, reducing the localization ambiguity inherent in one line of sight.

For forecasting, the important quantity is not only a CME's bulk speed but the location and strength of shocks, sheaths, and turbulent density structures that degrade radio navigation or foreshadow strong compression. Phase and Doppler statistics are especially suitable for automated quality flags because they are already present in tracking residuals. However, an operational threshold must be learned from many events and must condition on elongation, frequency, elevation, link mode, station weather, and solar-cycle background. The present case is evidence of capability, not an event-rate or false-alarm estimate.

5.4 Limitations

Five limitations define the interpretation.

First, the analysis uses published scan summaries rather than raw baseband or residual-phase series. We cannot alter detrending order, recompute spectra, inspect sub-scan intermittency, or model red-noise covariance. Second, the matched controls are days apart and use different uplink stations in some sessions; the multi-diagnostic and dual-receiver agreement mitigate but do not eliminate this noncontemporaneous design. Third, only four simultaneous station scans are available. Their CCC is high, yet exact permutation inference is underpowered. Fourth, the 0.50–0.60 AU crossing location is inherited from a WSA–ENLIL interpretation, and the radio line may sample an oblique CME flank. Our spatial scale is therefore radial-equivalent and conditional, not a fully deprojected three-dimensional thickness. Fifth, no in situ monitor sampled the same 0.5–0.6 AU chord, so the radio layer cannot be uniquely labeled as shock, sheath, or flux rope.

The uncertainty intervals quantify selected statistical and geometric inputs. They do not include all model discrepancy, catalog projection, or plasma-screen anisotropy. The explicit lower bound on global width and the decision to withhold bulk density are designed to prevent those unmodeled terms from being hidden inside a single precise number.

6. Conclusions

This reanalysis converts a previously reported radio detection into a calibration-resistant physical measurement of ICME structure. The evidence supports five conclusions.

1. The 6 April 2015 Mars Express radio link was disturbed across independent phase, Doppler, and spectral diagnostics. Relative to nearest same-station controls, the event enhancements are factors of about 3–5 in phase amplitude, 3–5 in Doppler noise, and 15–16 in spectral-peak power.
2. A blind BIC search resolves a 60 ± 20 min high-scattering interval from 06:40 to 07:40 UTC. Its phase-variance proxy is 2.37 times that of the adjoining ICME regimes, indicating a localized turbulent layer within a broader disturbance.
3. The radio signature is internally coherent: phase and Doppler noise co-vary at Badary ($r = 0.858$, permutation $p = 0.0024$), and simultaneous station measurements have CCC = 0.925. The four paired scans are too few for a strong stand-alone significance claim.
4. DONKI timing and the modeled crossing radius imply a path-averaged speed of 686 km s^{-1} (613–760), a radial-equivalent internal thickness of 0.016 AU (0.011–0.023), and a full disturbed-width lower bound of 0.055 AU.
5. The phase spectrum is near Kolmogorov. Absolute TEC and bulk density are not reproducibly determined by the archived numbers and are therefore not reported as physical measurements.

The central methodological result is that CME turbulence, propagation speed, and spatial scale can be inferred from an operational spacecraft carrier without depending on a disputed absolute TEC calibration. Future multi-link observations with open data and versioned processing can turn this proof of capability into a tomographic heliospheric sensor.

Open Research

Data Availability Statement

The radio measurements are numerical transcriptions of Tables 2 and 4 in Molera Calvés et al. (2017), available through the article DOI (https://doi.org/10.1002/2017SW001701) and the public CaltechAUTHORS record (https://authors.library.caltech.edu/records/z773c-3ny24). NASA CCMC DONKI documentation and the public web service are available at https://ccmc.gsfc.nasa.gov/tools/DONKI/. JPL Horizons API documentation is available at https://ssd-api.jpl.nasa.gov/doc/horizons.html. Frozen DONKI and Horizons responses, source checksums, the two radio CSV files, analysis code, and machine-readable results accompany this manuscript in the reproducibility package. The original article's Bitbucket data URL did not permit anonymous access when checked on 14 August 2026; raw baseband data were not used. Before journal submission, the accompanying package should be deposited in a DOI-minting repository.

Code Availability

The complete analysis is implemented in `analyze_radio_cme.py` with fixed random seed 20260814. It reproduces all reported statistics and figures from the packaged CSV/JSON/text inputs. Software environment and input SHA-256 hashes are recorded in the package.

Acknowledgments

This reanalysis uses measurements originally acquired by the Mars Express, ESA ground-station, PRIDE, Badary, and Hartebeesthoek teams; public CME information from NASA CCMC DONKI; and ephemerides from NASA/JPL Horizons. No funding source is asserted in this anonymous draft. Authors should add grant numbers and institution-specific acknowledgments before submission.

Author Contributions and Competing Interests

To be completed by the submitting authors. No contribution, funding, or conflict-of-interest statement has been fabricated for this anonymous draft.

Appendix A. Reproducibility Audit of the Published TEC Conversion

The audit below evaluates only arithmetic reproducibility. It does not attempt to reconstruct undocumented processing choices.

Quantity	Ht	Bd	Reproduction
Printed session σ_{Sc} [rad]	1.537	2.170	Source Table 2 / narrative
Arithmetic mean of Table 4 scans [rad]	1.9685	2.2487	Direct mean of 4 and 10 printed scans
Printed standard-mode equation, $2K_s\sigma_{Sc}$ [TECU]	6,178.7	8,723.4	$K_s=2010$ TECU rad⁻¹
Table 2 TEC [TECU]	3,074	4,340	Approximately $K_s\sigma_{Sc}$
Narrative / Table 5 TEC [TECU]	3,430	4,350	Not jointly reproduced by printed inputs

Table A1. Internal numerical audit. The discrepancy is isolated from all primary results by using radio-observable ratios, time structure, spectral slope, and catalog-conditioned kinematics.

The phase-amplitude means in Table 2 (1.96 ± 0.59 rad and 2.25 ± 0.56 rad) do reproduce the arithmetic means and dispersions of the Table 4 scan values to rounding. Thus the underlying scan transcription is self-consistent; the ambiguity concerns the separate σ_{Sc} summary and absolute TEC mapping. A future raw-data release should specify whether K_s is one-way or two-way, whether the factor of two is absorbed into its empirical value, which scan aggregation defines the session index, and how uplink/downlink correlation enters the calibration.

Appendix B. Statistical and Geometric Sensitivity

B1. Alternative Ht background

The primary Ht control is 4 April because it is the nearest same-station session and has the higher background phase amplitude. Using both 3 and 4 April as a pooled background increases, rather than removes, the event contrast. The qualitative conclusion is therefore not selected by control choice.

B2. Segmentation stability

All one-, two-, and three-regime partitions with a minimum of two scans per regime were enumerated. The preferred cuts occur after indices 4 and 7 of the ordered Bd series. Under parametric bootstrap draws from the fitted three-regime model, the exact partition is recovered 68.8% of the time and both cuts remain within one 20 min scan in 96.2%. Allowing one-scan regimes produces the same optimum; the minimum-length condition does not create the central layer.

B3. Spatial-scale interpretation

The reported 0.016 AU scale assumes frozen radial advection. If the scattering structure's normal is inclined to the radial velocity or if the line of sight sweeps appreciably across the front, the geometric thickness is $L_n = v_{rel} \Delta t \cos \alpha$, where v_{rel} is the relative pattern speed and α is the unknown angle between velocity and layer normal. Because the archived record does not constrain α, we report the radial-equivalent $v_{tr} \Delta t$ and do not apply an incidence-angle correction.

References

Armstrong, J. W. (1998). Radio wave phase scintillation and precision Doppler tracking of spacecraft. *Radio Science, 33*(6), 1727–1738. https://doi.org/10.1029/98RS02317

Asmar, S. W., Lazio, J., Atkinson, D. H., et al. (2019). Future of planetary atmospheric, surface, and interior science using radio and laser links. *Radio Science, 54*, 365–377. https://doi.org/10.1029/2018RS006663

Bocanegra-Bahamón, T. M., Molera Calvés, G., Gurvits, L. I., Duev, D. A., Pogrebenko, S. V., Cimò, G., Dirkx, D., & Rosenblatt, P. (2018). Planetary Radio Interferometry and Doppler Experiment (PRIDE) technique: A test case of the Mars Express Phobos fly-by. II. Doppler tracking: Formulation of observed and computed values, and noise budget. *Astronomy & Astrophysics, 609*, A59. https://doi.org/10.1051/0004-6361/201731524

Cane, H. V., & Richardson, I. G. (2003). Interplanetary coronal mass ejections in the near-Earth solar wind during 1996–2002. *Journal of Geophysical Research: Space Physics, 108*(A4), 1156. https://doi.org/10.1029/2002JA009817

Chen, P. F. (2011). Coronal mass ejections: Models and their observational basis. *Living Reviews in Solar Physics, 8*, 1. https://doi.org/10.12942/lrsp-2011-1

Duev, D. A., Molera Calvés, G., Pogrebenko, S. V., Gurvits, L. I., Cimò, G., & Bocanegra Bahamón, T. (2012). Spacecraft VLBI and Doppler tracking: Algorithms and implementation. *Astronomy & Astrophysics, 541*, A43. https://doi.org/10.1051/0004-6361/201218885

Edwards, J., Molera Calvés, G., Kummamuru, P., Md Said, M. D., & Ma, M. (2025). Studying the inner heliosphere using radio signals transmitted from spacecraft orbiting Mars. *Space Weather, 23*, e2024SW004225. https://doi.org/10.1029/2024SW004225

Edwards, J., Molera Calvés, G., Morgan, J., & Cheung, M. (2026). An analysis of a coronal mass ejection leading edge by means of multi-spacecraft-in-beam phase scintillation. *Publications of the Astronomical Society of Australia, 43*, e004. https://doi.org/10.1017/pasa.2025.10134

Giorgini, J. D., Yeomans, D. K., Chamberlin, A. B., et al. (1996). JPL's on-line Solar System data service. *Bulletin of the American Astronomical Society, 28*, 1158.

Hewish, A., Scott, P. F., & Wills, D. (1964). Interplanetary scintillation of small diameter radio sources. *Nature, 203*, 1214–1217. https://doi.org/10.1038/2031214a0

Kay, C., Opher, M., & Evans, R. M. (2015). Global trends of CME deflections based on CME and solar parameters. *The Astrophysical Journal, 805*, 168. https://doi.org/10.1088/0004-637X/805/2/168

Kolmogorov, A. N. (1991). The local structure of turbulence in incompressible viscous fluid for very large Reynolds numbers. *Proceedings of the Royal Society A, 434*, 9–13. https://doi.org/10.1098/rspa.1991.0075

Kummamuru, P., Molera Calvés, G., Cimò, G., et al. (2023). A monitoring campaign (2013–2020) of ESA's Mars Express to study interplanetary plasma scintillation. *Publications of the Astronomical Society of Australia, 40*, e013. https://doi.org/10.1017/pasa.2023.12

Lin, L. I.-K. (1989). A concordance correlation coefficient to evaluate reproducibility. *Biometrics, 45*(1), 255–268. https://doi.org/10.2307/2532051

Molera Calvés, G., Pogrebenko, S. V., Cimò, G., et al. (2014). Observations and analysis of phase scintillation of spacecraft signal on the interplanetary plasma. *Astronomy & Astrophysics, 564*, A4. https://doi.org/10.1051/0004-6361/201322925

Molera Calvés, G., Kallio, E., Cimò, G., et al. (2017). Analysis of an interplanetary coronal mass ejection by a spacecraft radio signal: A case study. *Space Weather, 15*, 1523–1534. https://doi.org/10.1002/2017SW001701

Odstrčil, D. (2003). Modeling 3-D solar wind structure. *Advances in Space Research, 32*(4), 497–506. https://doi.org/10.1016/S0273-1177(03)00332-6

Pätzold, M., Hahn, M., Tellmann, S., Häusler, B., Bird, M. K., Tyler, G. L., Asmar, S. W., & Tsurutani, B. T. (2012). Coronal density structures and CMEs: Superior solar conjunctions of Mars Express, Venus Express, and Rosetta: 2004, 2006, and 2008. *Solar Physics, 279*, 127–152. https://doi.org/10.1007/s11207-012-9991-y

Schwarz, G. (1978). Estimating the dimension of a model. *The Annals of Statistics, 6*(2), 461–464. https://doi.org/10.1214/aos/1176344136

Vršnak, B., Žic, T., Vrbanec, D., et al. (2013). Propagation of interplanetary coronal mass ejections: The drag-based model. *Solar Physics, 285*, 295–315. https://doi.org/10.1007/s11207-012-0035-4

You, X. P., Hobbs, G., Coles, W. A., et al. (2012). Measurement of the electron density and magnetic field of the solar wind using millisecond pulsars. *Monthly Notices of the Royal Astronomical Society, 422*, 1160–1165. https://doi.org/10.1111/j.1365-2966.2012.20688.x